CHEMISTRY & CHEMICAL TECHNOLOGY

Vol. 9, No. 4, 2015 Chemistry

Maralla Yadagiri[1], Singuru Ramakrishna[2], Gundeboina Ravi[2], Palla Suresh[2], Kurra Sreenu[2], Dodle Jaya-Prakash[1] and Muga Vithal[2]

PREPARATION, CHARACTERIZATION AND PHOTOCATALYTIC STUDIES OF $Cr_2(MoO_4)_3$ AND NITROGEN-DOPED $Cr_2(MoO_4)_3$

[1]University College of Technology, Osmania University, Hyderabad-500 007, India
[2]Department of Chemistry, Osmania University, Hyderabad-500 007, India; mugavithal@gmail.com

Received: October 08, 2014 / Revised: November 21, 2014 / Accepted: February 23, 2015

Abstract. $Cr_2(MoO_4)_3$ and N-doped $Cr_2(MoO_4)_3$ are prepared by sol-gel and solid state methods, respectively. These molybdates are characterized by powder X-ray diffraction, scanning electron microscopy, energy dispersive spectroscopy, thermogravimetric analysis, FT-IR and UV-visible diffuse reflectance spectroscopy. The photodegradation of methylene blue solution was investigated in the presence of these oxides.

Keywords: molybdate, powder XRD, methylene blue, photodegradation.

1. Introduction

Methylene blue (MB) is widely used in the textile industry as a dying agent. It is soluble in water, toxic and non-biodegradable. A large volume of colored organic dyes, including MB is released into aquatic habitats by textile industries causing severe environmental pollution. A number of physical and chemical methods such as adsorption, flocculation, reverse osmosis, precipitation, air stripping, and ultrafiltration have been developed for decolorization of polluted water. Nevertheless, these methods are expensive and transfer the pollutants into sludge that gives rise to new pollutants. Advanced oxidation processes (AOPs), a group of established treatment methods which rely on the generation of OH radicals for degradation of pollutants, are found to be effective both from the economic and energy points of view to address the decolorization of polluted water. Semiconductor mediated visible light driven photocatalysis, one of the AOP, is considered as one of the promising and green chemical process for wastewater management. Titanium dioxide, a wide bandgap material, has been extensively used as photocatalyst due to its remarkable properties such as chemical stability, cost, activity under a wide range of pH and efficiency [1, 2]. One of the main drawbacks of TiO_2 is its large bandgap which restricts its use in UV light only. Therefore, the focus has been shifted to visible light driven semiconducting materials for harvesting the solar energy for photocatalytic applications including the degradation of pollutants.

Binary and ternary transition metal oxides have been considered as potential photocatalysts for dye degradations [3-5]. The properties of these oxides can be tailored by substituting the anions and/or cations in their lattices [6, 7]. Molybdates and tungstates of composition $A_2M_3O_{12}$ (M = Mo, W) have been extensively investigated for their negative thermal expansion (NTE) phenomena. The structure of these materials consists of corner-sharing AO_6 octahedra and MO_4 tetrahedra. Several studies on the thermal expansion properties of tungstates and molybdates of $A_2M_3O_{12}$ family and their solid solutions have been reported [8-13]. The A^{3+}cation in $A_2M_3O_{12}$ can be occupied by a transition or rare earth cation indicating its compositional flexibility. Therefore, these materials are promising for tailoring of new materials with a controllable coefficient of thermal expansion [14, 15].

Chromium molybdate ($Cr_2(MoO_4)_3$) is one of the $A_2M_3O_{12}$ structure type molybdates, which exhibits interesting magnetic, electrical and catalytic properties. It is prepared by solid state synthesis, precipitation method

or thermal decomposition of chromate and molybdate solutions [9, 16-18]. The method of preparation is found to influence its properties significantly. Although the magnetic and electric properties of $Cr_2(MoO_4)_3$ have been extensively studied, the reports on its catalytic properties are limited [19-21]. The photocatalytic activity of $Cr_2(MoO_4)_3$ to our knowledge is not reported. In this paper we report preparation, characterization and photocatalytic activity against MB degradation of $Cr_2(MoO_4)_3$ and its N-doped analogue.

2. Experimental

2.1. Preparation of $Cr_2(MoO_4)_3$

Parent $Cr_2(MoO_4)_3$ is prepared by a sol-gel method using $Cr(NO_3)_3 9H_2O$, $(NH_4)_6Mo_7O_24 4H_2O$, aqueous NH_3, citric acid and ethylene glycol. Stoichiometric quantities of $Cr(NO_3)_3 9H_2O$ and $(NH_4)_6Mo_7O_{24}\cdot 4H_2O$ were first dissolved in double distilled water separately and labeled as "solution A" and "solution B", respectively. "Solutions A" was slowly added to "solution B". The chelating agent, citric acid, was added to this resultant solution. The molar ratio of citric acid to metal ions was 2:1. The pH of the ensuing metal citrate solution was attuned to 6–7 by adding dilute ammonia solution. The solution was then slowly evaporated on a hot plate till a viscous liquid was obtained. At this stage the gelating reagent, ethylene glycol, was added to the solution. The molar ratio of citric acid to ethylene glycol was 1.0:1.2. This mixture was heated at 373 K for 2–3 h under constant stirring. The temperature was increased to 433–453 K at the onset of solidification. The ensuing solid porous mass was crushed in an agate mortar using spectral grade acetone. The resultant black powder was heated in a muffle furnace at 773 K for 2 h. The obtained powder was brown in color and designated as CMO.

2.2. Preparation of N-doped $Cr_2(MoO_4)_3$

The N-doped CMO ($Cr_2(MoO_{4-x}N_y)_3$) was obtained by heating a mixture of CMO and urea at 673 K for 2 h in a muffle furnace. The weight ratio of CMO to urea was 1:2. The resultant powder was washed several times with deionized water to remove excess unreacted urea and by-products. The N-doped CMO was found to be blackish brown in color and designated as CMON.

2.3. Characterization

The powder X-ray diffractograms were recorded on Rigaku miniflex 600 powder X-ray diffractometer at room temperature in the 2θ range 10–80° for phase confirmation using Cu Kα radiation of wavelength 1.5406 Å. The step size and scan step time were 0.02^0 and 0.15 s, respectively. Thermogravimetric analysis (TGA) was performed using a Shimadzu differential thermal analyzer (DTG-60H) with a heating rate of 15 K/min. The SEM-EDS images were recorded on the HITACHI SU-1500 variable pressure scanning electron microscope (VP-SEM). Infrared spectra were recorded in the form of KBr pellets in the wave number range 1000–400 cm^{-1} using JASCO IR-5300 spectrometer. JASCO V-650 UV-vis spectrophotometer was used for UV-vis diffuse reflectance spectra (DRS) measurements in the range of 200–900 nm. $BaSO_4$ was used as the reflectance standard.

2.4. Photocatalytic Activity Measurement

Photoactivity of these samples was studied by photodegradation of methylene blue (MB) under visible light irradiation employing a 300 W lamp ($380 < \lambda < < 840$ nm) in HEBER visible annular type photoreactor. In a typical process, the catalyst (50 mg) was added to 50 ml of MB aqueous solution (10 mg/l), in cylindrical-shaped glass reactor at room temperature in air. The suspension was stirred in the dark for 60 min to establish adsorption–desorption equilibrium. At regular time intervals of 30 min, about 3–5 ml of the solution was collected and centrifuged to remove the catalyst particles and analyzed by JASCO V650 UV-vis spectrophotometer at λ_{max} (664 nm). The degraded amount of MB is reported as $d = \frac{(C_0 - C)}{C_0}$ where C is the concentration of MB at each irradiated time and C_0 is the concentration of MB at equilibrium.

2.5. Determination of Methylene Blue Concentration

The concentration of MB in aqueous solutions was determined by measuring absorbance at its λ_{max} (664 nm) using the calibration curve. Fig. 1 shows the graphical relationship between concentration of MB and absorbance at 664 nm for calibration solutions. It is found that the calibration curve obeys the Beer's law ($A = \varepsilon lc$) in the concentration range of 0.0–10 $mg\cdot l^{-1}$.

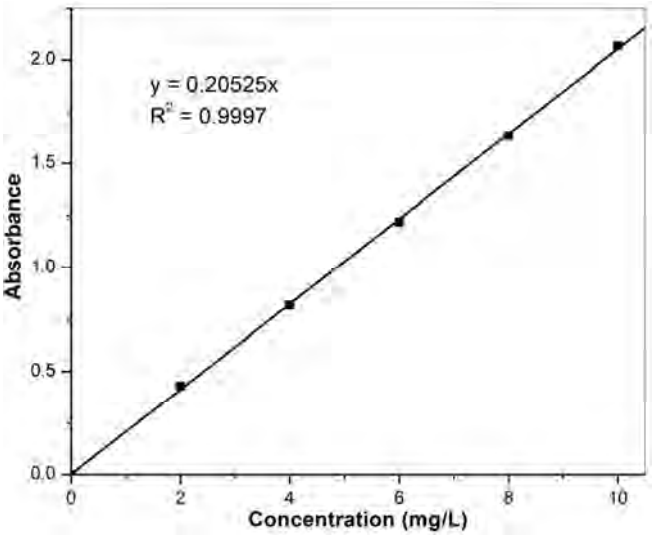

Fig. 1. Calibration curve of methylene blue

3. Results and Discussion

3.1. Powder XRD

The room temperature powder XRD patterns of CMO and CMON are recorded for phase conformation (Fig. 2). The powder patterns of CMO are consistent with reported data [JCPDF-20-0310] and free from impurities. The powder pattern of CMON is similar to that of CMO. Nevertheless, when plotted in an expanded scale, the diffraction peaks show a systematic shift towards lower 2θ value indicating a change in unit cell parameters and the substitution of nitrogen into the CMO lattice (Fig. 3). As the ionic radius of N^{3-} (0.171 nm) is higher than that of O^{2-} (0.140 nm), partial replacement of O by N should increase the unit cell parameter. The *d*-lines of CMO and CMON are refined by least square fitting the powder data, using POWD software. Both samples crystallized in orthorhombic lattice with space group *pbcn*. The observed changes in unit cell lengths and unit cell volume are due to the partial substitution of nitrogen into MO_4 tetrahedra (Table 1). The observed and calculated *d*-values for the CMO and CMON along with *hkl* values are given in Table 2. The crystallite size of all powders was calculated from the line width of the intense diffraction line (103) using the Scherer's formula [22]:

$$t = \frac{0.9\,l}{b\cos q}$$

where t is the thickness in angstrom (Å) and corresponds to the crystallite diameter assuming a spherical shape; λ is the wave length of the X-ray used; θ is the Bragg angle and β is the full width at half maximum measured in radians of intense line in the powder XRD pattern.

The crystallite sizes of the CMO and CMON were found to be 47 and 44 nm, respectively.

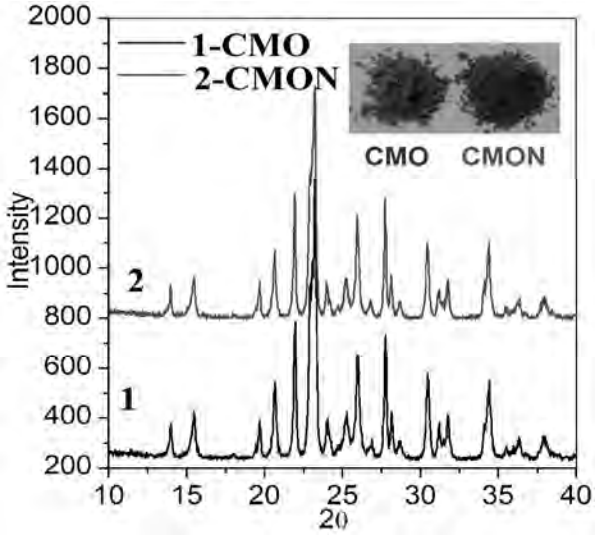

Fig. 2. Powder XRD patterns of CMO (1) and CMON (2)

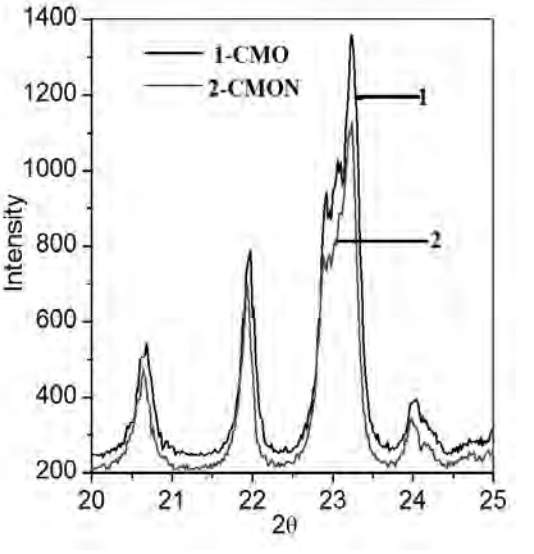

Fig. 3. The observed shift of *d*-spacing between CMO (1) and CMON (2)

Table 1

Refined unit cell parameters for CMO and CMON

Unit cell parameters	CMO	CMON
a (Å)	12.5784	12.5784
b (Å)	8.8985	8.9260
c (Å)	9.1249	9.1603
α (°)	37.50	37.50
β (°)	74.93	74.47
γ (°)	71.26	70.71
V $(Å)^3$	1021.34	1028.47

Table 2

The observed and calculated *d* values for CMO and CMON along with their *hkl* values

hkl	CMO		CMON	
	d_{obs}	d_{cal}	d_{obs}	d_{cal}
011	6.3380	6.3707	6.3482	6.3929
111	5.7371	5.6833	5.7421	5.699
211	4.5151	4.4757	4.5182	4.4833
102	4.2999	4.2890	4.3049	4.3037
012	4.0499	4.0599	4.0547	4.0750
112	3.8463	3.8636	3.8503	3.8766
202	3.7012	3.6930	3.7056	3.7024
311	3.5262	3.5024	3.5309	3.5060
212	3.4297	3.4109	3.4328	3.4199
221	3.3214	3.3747	3.3253	3.3825
022	3.1675	3.1854	3.2164	3.1964
122	3.1122	3.0879	3.1132	3.0980
312	2.9329	2.9166	2.9354	2.9222
013	2.8635	2.8781	2.8640	2.8495
411	2.8177	2.8198	2.8198	2.8217
213	2.6098	2.6171	2.6120	2.6253
421	2.4739	2.4719	2.4755	2.4750

3.2. Thermogravimetric Analysis

Thermogravimetric (TG) profile of CMON is shown in Fig. 4. This profile is characterized by two significant weight change regions. In the temperature region of 303–673 K the observed weight loss for CMON is 0.32 %. This weight loss may be attributed to adsorbed and lattice water as they were extracted from water. In the 673–1073 K region CMON sample registered a weight gain of 0.11 %. It is well known that N-doped oxides gain weight on heating to above 673 K due to the release of gaseous nitrogen and becomes pure oxides [7]. Based on the TG profiles, the molecular formula of CMON can be written as $Cr_2(MoO_{4-x}N_y)_3$ $0.01H_2O$ (wt % of N is 0.11).

3.3. SEM-EDS

The morphology of the CMO and CMON was studied by scanning electron microscope (SEM) (Fig. 5). The SEM image of both CMO and CMON show spherical shaped irregular size micro crystallites with considerable agglomeration. An estimation of nitrogen content in CMON was also obtained from EDS measurements (Fig. 5c). From the EDS data, the nitrogen content (wt %) for CMON was found to be 0.15. This result is comparable with the nitrogen weight percent obtained from TGA results.

3.4. FT-IR Spectra

The IR spectra of CMO and CMON are shown in Fig. 6. These spectra are comparable with reported IR data of $Cr_2(MoO_4)_3$ [23]. The broad band at 970 cm^{-1} is due to activation of ν_1 vibrations and bands in the range of 780–850 cm^{-1} are attributed to ν_3 vibrations of the distorted MoO_4 tetrahedra [21]. Further, when Mo–O bonds are replaced by Mo–N, the bond length increases (due to higher ionic radius of N^{3-}) leading to a decrease in the force constant. Lower force constant results in a lower stretching or bending vibrational frequency. The observed shift in the band positions is in accordance with this argument [24].

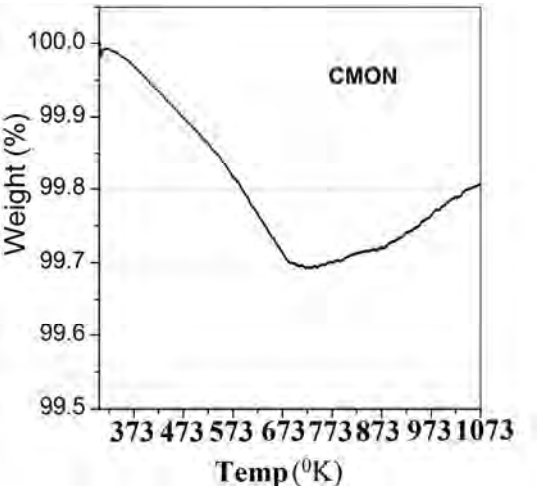

Fig. 4. Thermogravimetric profiles of N-doped CMO

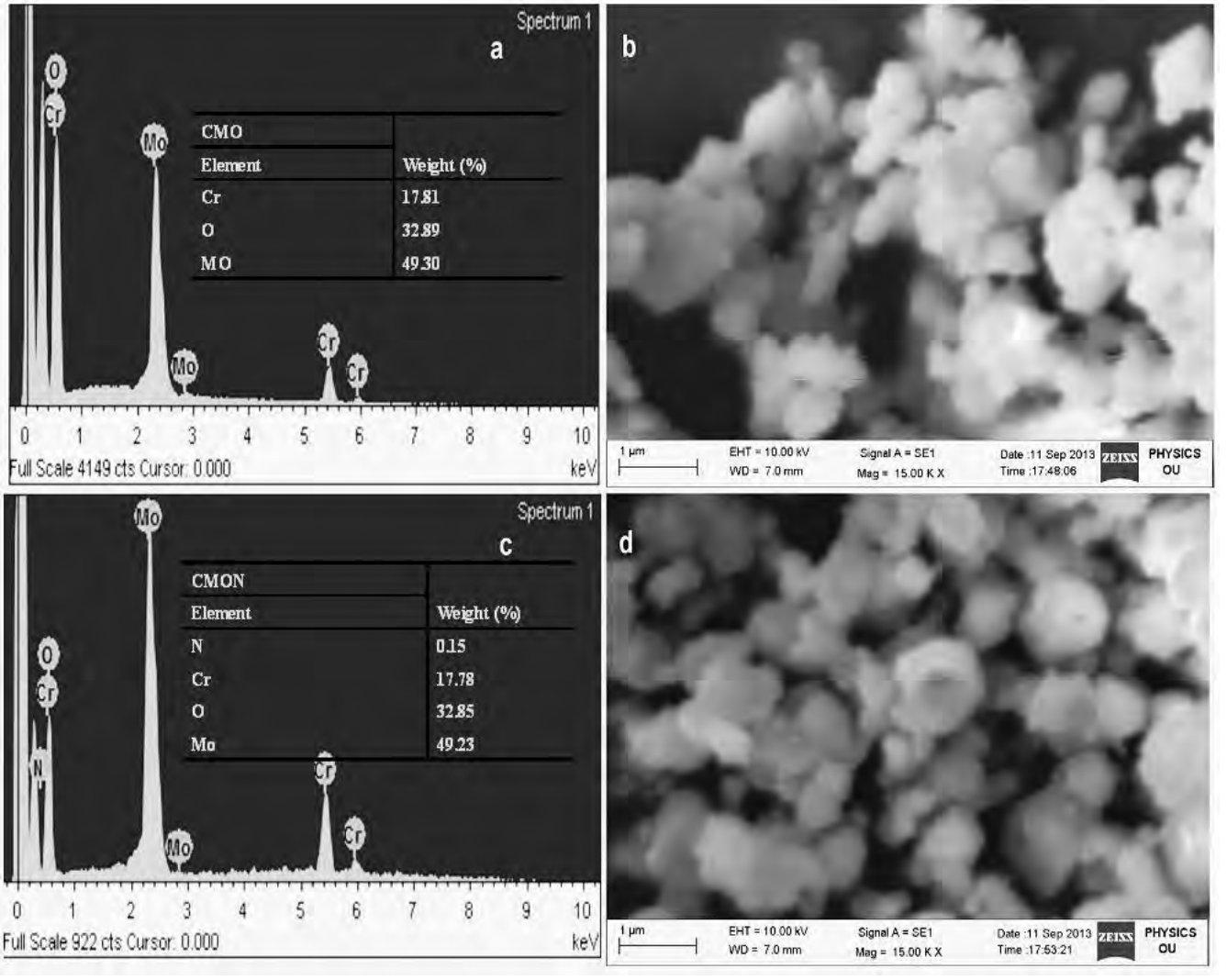

Fig. 5. EDS profiles of CMO (a) and CMON (c); SEM images of CMO (b) and CMON (d)

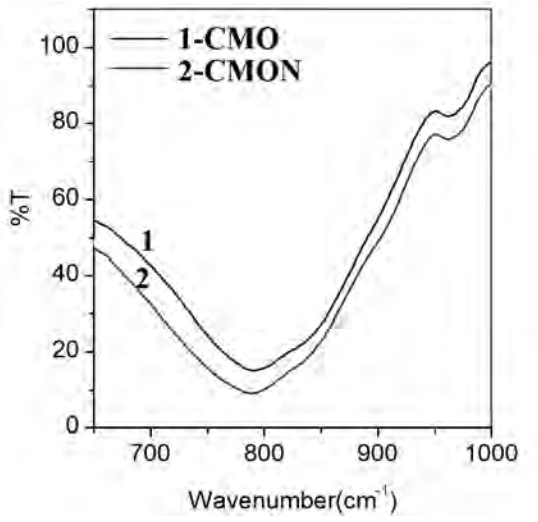

Fig. 6. The FT-IR spectra of CMO (1) and CMON (2)

3.5. UV-visible Diffuse Reflectance Spectra Analysis

The light absorption properties of the CMO and CMON are investigated. Fig. 7 shows the diffused reflectance spectra (DRS) of these materials in the range of 200–900 nm. The spectra were characterized by peaks belonging to Cr^{3+} in the visible region and steeply increasing profile in the lower wavelength region. Trivalent chromium ($3d^3$) with a ground state of $^4A_2$ (F) is expected to give three spins allowed transitions (a, b, c) and a spin forbidden transition (d) as shown below:

$$^4A_{2g}(F) \rightarrow {}^4T_{2g}(F) \quad \text{(a)}$$

$$^4A_{2g}(F) \rightarrow {}^4T_{1g}(F) \quad \text{(b)}$$

$$^4A_{2g}(F) \rightarrow {}^4T_{1g}(P) \quad \text{(c)}$$

$$^4A_2 \rightarrow {}^2E \quad \text{(d)}$$

The transitions (a), (b) and (d) occur at ≈ 685, 490 and 745 nm, respectively. The transition (a), *viz.* $^4A_{2g}(F) \rightarrow {}^4T_{2g}(F)$ corresponds to 10Dq. The transition (c), *i.e.* $^4A_{2g}(F) \rightarrow {}^4T_{1g}(P)$ is overlapped with charge transfer transition and hence is not detectable. The energies of electronic states *E* of the Cr^{+3} are influenced by the crystal field strength *Dq* and Racah parameters (*B* and *C*). The interrelation of these parameters, neglecting spin-orbit effects, is given by the Tanabe-Sugano strong field matrices [25]. The Racah parameters *B* and *C* are evaluated as follows. Let the energy difference between transitions (b) and (a) be δ. The parameter *B* can be estimated using the equation:

$$\frac{B}{Dq} = \frac{\left(\frac{d}{Dq}\right)^2 - 10\left(\frac{d}{Dq}\right)}{15\left(\frac{d}{Dq} - 8\right)}$$

The value of *C* was found from the following equation [26]:

$$E(^2E) \approx 3.05C + 7.9B - 1.8\frac{B^2}{d}$$

The values of *Dq*, *B*, *Dq*/*B*, *C* and *C*/*B* obtained for CMO are 1459, 580, 2.51, 2932 and 5.05 cm^{-1}, respectively. The value of *B* is 918 cm^{-1} for the Cr^{3+} free ion [27]. Thus, the observed *B* value is decreased by about 44 %. The reduction in *B* value might be due to bonding effects in this oxide. It is seen that, in the Tanabe-Sugano diagram, the crossing of the ^2E_g and $^4T_{2g}$ levels occurs near $Dq/B = 2.3$. The value higher than 2.3 for *Dq*/*B* corresponds to strong ligand field sites [28]. Thus, the Cr^{3+} ion in CMO is in strong ligand field sites. The substitution of nitrogen into CMO lattice does not alter the absorption band positions considerably.

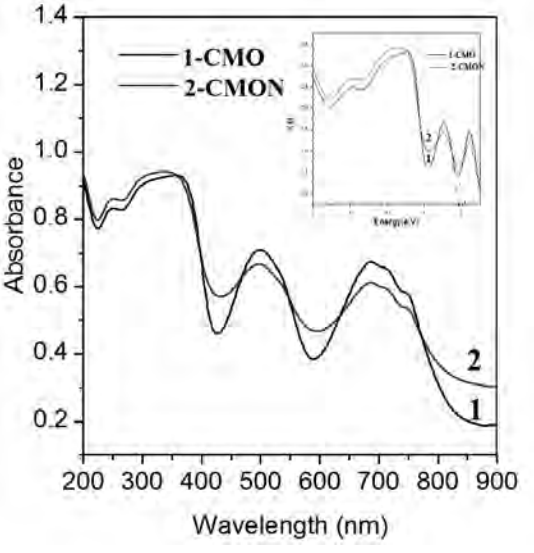

Fig. 7. UV-visible DRS of CMO (1) and CMON (2); inset shows the KM plot for CMO (1) and CMON (2)

The absorption band edge of the samples was obtained by extrapolating the horizontal and sharply rising part of the curves onto the wavelength axis. The edge of each absorption band was shifted towards longer wavelength side for CMON indicating the change in the band structure due to substitution of nitrogen into CMO. The red shift of CMON compared to CMO is further endorsed by a change in the color of the samples. The bandgap energy of semiconducting oxides can be obtained

from the Kubelka-Munk plot of $(Khv)^{1/2}$ *vs.* hν. Extrapolation of the linear part of the plot to $(Khv)^{1/2} = 0$ (*i.e.* to the X-axis) provides an estimation of the bandgap energy. Fig. 7 (inset) shows the Kubelka-Munk (KM) plot for both CMO and CMON samples and the estimated bandgap for these samples are found to be 2.08 and 1.89 eV, respectively. Thus, the introduction of nitrogen into the CMO lattice reduces the bandgap energy considerably as seen from the red shifts of the absorption band edge. It can be ascribed to the widening of the valence band, resulting from the hybridization of N 2*p* and O 2*p* [7].

3.6. Photodegradation of Methylene Blue

The photocatalytic activity of CMO and CMON is evaluated by degradation of MB under the visible light irradiation. The degradation of both the samples was monitored by measuring the optical density (at 664 nm). Initially, the dark reaction was carried out for 60 min to attain the adsorption-desorption equilibrium in dye-catalyst suspension. Both CMO and CMON samples have adsorbed about 10–16 % of MB in the dark reaction. Under the light irradiation, it is seen that the degradation of MB increased with an increase in the irradiation time (Fig. 8).

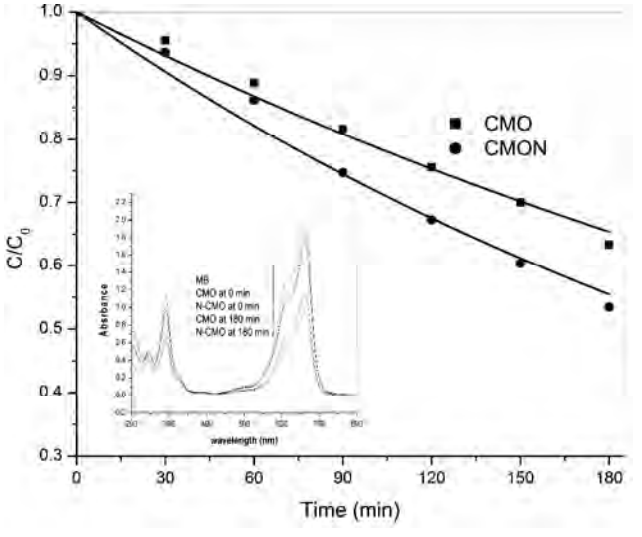

Fig. 8. The degradation of MB solution (C_0 (MB) = 10 mg/l) in the presence of CMO and CMON.
Inset shows the UV-vis spectra of MB at different time intervals in the presence of CMO and CMON

Fig. 8 (inset) shows the UV-visible spectra of MB at different time intervals of irradiation. The absorption spectrum of MB is characterized by a medium band at ~300 nm and a strong band at ~675 nm with a shoulder at ~600 nm. The band at ~300 nm is attributed to the aromatic ring, whereas the overlapping bands at ~ 600 and ~ 675 are assigned to conjugated π-system [29]. The decrease in absorbance of MB with increasing irradiation time indicates that both the materials in the present study have exhibited photoactivity against MB degradation under visible light irradiation. The range of MB degradation after 180 min of irradiation seen for the CMO and CMON is 37 and 47 %, respectively. Photocatalytic processes are based on electron hole pairs generated by means of photo excitation. The photoinduced electron and hole could migrate to the surface to react with the adsorbed reactants in the desired process, or undergo undesired recombination. Therefore, the generation and separation of photoinduced electron hole pairs are the key factors in a photocatalytic reaction. The possible photocatalytic degradation mechanism of MB under visible light irradiation is as follows:

Ø In the presence of light, electrons are excited from the valence band to the conduction band of the catalyst (CMO/CMON), leaving a hole in the valence band.

$$CMO/CMON + h\nu \rightarrow e^-_{CB} + h^+_{VB} \quad (1)$$

Ø The excited electrons and holes can combine with surface OH^- species and adsorbed oxygen to form the $^{\bullet}OH$ and $O_2^{\bullet -}$, respectively. Subsequently, these $^{\bullet}OH$ and $O_2^{\bullet -}$ react with dye molecules and degrade them into simple inorganic minerals.

$$OH^- + h^+_{VB} \rightarrow {}^{\bullet}OH + H^+ \quad (2)$$

$$O_2 + e^-_{CB} \rightarrow O_2^{\bullet -} \quad (3)$$

$$O_2^{\bullet -} + {}^{\bullet}OH + Dye \rightarrow Byproducts \quad (4)$$

The photocatalytic activity of a material depends on several factors such as surface structure, degree of crystallinity, surface area, structure of material, adsorption ability of the pollutant, and bandgap energy of the material. The physical processes, including light absorption, transport of charge carriers and recombination rate of photogenerated electron-hole pairs influence photocatalytic efficiency of a photocatalyst. The bandgap energy of photocatalyst plays a key role in these processes. In the present study, the improved photoactivity for N-doped oxide may be attributed to (a) decrease in the band gap energy of CMON resulting in an increase in the number of absorbed photons and (b) defects created in the lattice due to the incorporation of nitrogen leading to a reduction in the electron-hole recombination rate.

3.6.1. Kinetic study to predict the rate constant for the reaction

The kinetics of MB degradation in the presence of both the catalysts was also studied. The degradation reaction of MB with CMO and CMON shows pseudo first order kinetics (Langmuir-Hinshelwood model) [30]. The results were nearly consistent with linear equation $\ln(\frac{C}{C_0}) = -kt$.

Fig. 9 represents a linear correlation, suggesting that the degradation reaction is of the first order. The correlation coefficient R can be calculated using the following equation:

$$R = \frac{n \cdot \sum(x_i \cdot y_i) - \sum(x_i) \cdot \sum(y_i)}{\sqrt{\left(n \cdot \sum(x_i^2) - \left(\sum(x_i)\right)^2\right) \cdot \left(n \cdot \sum(y_i^2) - \left(\sum(y_i)\right)^2\right)}}$$

The slope of the linear line indicates the first order rate constant k. Standard deviations for the first order rate constants were given with the confidence level of 0.95 (95 %) according to the general expression $k = k_{mean} \pm \Delta k$ and Student's statistics is used in the calculation of confidence intervals Δk. The kinetic parameter k and square of correlation coefficients for both photocatalysts are given in Table 3.

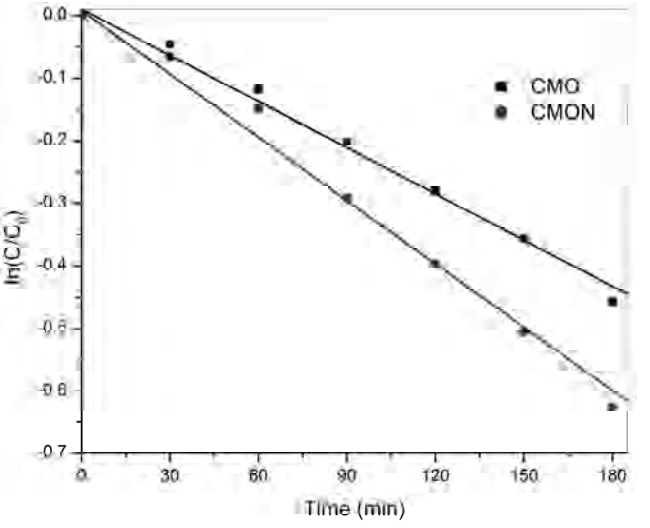

Fig. 9. The kinetics plot for the MB degradation in the presence of CMO and CMON

Table 3

First order rate constant k for the MB photodegradation reaction in the presence of CMO and CMON

Photocatalyst (Dye)	First order rate constant, $k = k_{mean} \pm \Delta k$, min^{-1}	Square of correlation coefficient R^2
CMO (MB)	0.00239±0.00021	0.998
CMON (MB)	0.00333±0.00032	0.997

4. Conclusions

Nitrogen doped $Cr_2(MoO_4)_3$ is prepared by a facile solid state reaction method using urea as a source of nitrogen. Powder XRD patterns confirm its phase formation. CMON is crystallized in orthorhombic lattice. Based on the TGA and EDS profiles, the nitrogen content in CMON was found to be in the range of 0.11–0.15 wt %. The incorporation of nitrogen into CMO lattice is confirmed from (i) shift in the *d* lines of powder patterns; (ii) the presence of N peak in its EDS profile; (iii) change in the color of the samples; and (iv) shift in the absorption edge in UV-visible DRS profiles. The bandgap energy of N doped CMO is reduced by about 0.2 eV. The nitrogen doped CMO has shown higher photoactivity against the methylene blue degradation under visible light irradiation. The MB degradation in the presence of CMO and CMON follows pseudo first order kinetics.

Acknowledgements

The authors gratefully acknowledge the financial assistance from the Department of Science & Technology (DST), New Delhi under FIST and University Grants Commission (UGC), New Delhi under UPE-FAR schemes. M. Yadagiri thanks Ministry of Human Resource Development, Government of India for the project assistantship under Technical Education Quality Improvement Program II (TEQIP II). The authors also acknowledge Dr. Igor Poluyuzhin (Lviv Polytechnic National University, Lviv, Ukraine) for the help in the calculations of rate constant and correlation coefficient values.

References

[1] Gaya U., Abdullah A., Zainal Z. and Hussein M.: J. Hazard. Mater., 2009, **168**, 57.

[2] Ghosh J., Sui R., Langford C. *et al.*: Water Res., 2009, **43,** 4499.
[3] He H. and Chen P.: Chem. Eng. Comm., 2012, **199**, 1543.
[4] Stoyanova M. and Christoskova S.: Cent. Eur. J. Chem., 2011, **9**, 1000.
[5] Singh J. and Uma S.: J. Phys. Chem. C, 2009, **113,** 12483.
[6] Ravi G., Veldurthi N., Palla S. *et al.*: Photochem. Photobiol., 2013, **89**, 824.
[7] Reddy J., Ravi G., Veldurthi N. *et al.*: Z. Anorg. Allg. Chem., 2013, **639**, 794.
[8] Haijun Z., Qing Z., Honglin D. and Quanli J.: Chem. Eng. Comm., 2008, **195**, 243.
[9] Peng J., Wu M., Wang H. *et al.*: J. Alloys. Compd., 2008, **453**, 49.
[10] Wu M., Peng J., Cheng Y. *et al.*: Solid State Sci., 2006, **8**, 665.
[11] Wu M., Cheng Y., Peng J. *et al.*: Mater. Res. Bull., 2007, **42**, 2090.
[12] Wu M., Peng J., Cheng Y. *et al.*: Mater. Sci. Eng. B, 2007, **137**, 144.
[13] Cheng Y., Wu M., Peng J. *et al.*: J. Solid State Sci., 2007, **9**, 693.
[14] Tao J. and Sleight A.: J. Solid State Chem., 2003, **173**, 442.
[15] Evans J., Mary T. and Sleight A.: J. Solid State Chem., 1997, **133**, 580.
[16] Doyle W., McCurie G. and Clark G.: J. Inorg. Nucl. Chem., 1966, **28**, 1185.
[17] Walczak J., Kurzawa M. and Filipek E.: Thermochim. Acta, 1989, **150**, 133.
[18] Evans J.: J. Chem. Soc. Dalton Trans., 1999, 3317.
[19] Verma S., Verma B. and Lal H.: J. Mater. Sci. Lett., 1986, **5**, 783.
[20] Klissueski D. and Kancheva M.: Studies in Surf. Sci. Catalysis, 1981, **7**, 1074.
[21] Battle P., Cheetham A., Harrison W. *et al.*: J. Solid State Chem., 1985, **58**, 221.
[22] Vogel A..: Textbook of Quantitative Chemical Analysis. Longman Group Ltd, Harlow 1989.
[23] Clark G. and Doyle W.: Spectrochim. Acta, 1966, **22**, 1441.
[24] Yang N., Li G., Yang X. *et al.*: J. Chem. Soc. Dalton Trans., 2011, **40**, 3459.
[25] Tanabe Y. and Sugano S.: J. Phys. Soc. Jpn., 1954, **9**, 753.
[26] Henderson B. and Imbush G.: Optical Spectroscopy of Inorganic Crystals. Oxford University Press, Oxford 1989.
[27] Orton J.: An Introduction to Transition Group Ions in Crystals. ILIFFE Book Ltd, London 1968.
[28] Long X., Lin Z., Hu Z. *et al.*: J. Alloy. Compd., 2002, **347**, 52.
[29] Ravi G., Palla S., Reddy J. *et al.*: Int. J. Green Nanotechn., 2012, **4**, 360.
[30] Liu Y., Chen X., Li J. and Burda C.: Chemosphere, 2005, **61**, 11.

ПІДГОТОВКА, ХАРАКТЕРИСТИКИ І ФОТОКАТАЛІТИЧНІ ДОСЛІДЖЕННЯ $Cr_2(MoO_4)_3$ і НІТРОГЕН-ВМІСНОГО $Cr_2(MoO_4)_3$

Анотація. *За допомогою золь-гель методу і методу твердого стану одержано $Cr_2(MoO_4)_3$ і N-вмісний $Cr_2(MoO_4)_3$, відповідно. З використанням порошкової рентгенівської дифракції, скануючої електронної мікроскопії, енергодисперсійної спектроскопії, термогравіметричного аналізу, Фур'є-спектроскопії та УФ-спектроскопії дифузного відбиття проведено аналіз одержаних молібдатів. У присутності цих сполук досліджено фотодеградацію метиленового синього.*

Ключові слова: *молібдат, порошкова рентгенівська дифракція, метиленовий синій, фотодеградація.*